

## Preparation and performance of PAA-g-MWCNTs incorporated PVDF composite membrane using as dye adsorbent

Guanglin Wang, Yangyang Huan, Guangfen Li\*

State Key Laboratory of Separation Membranes and Membrane Processes, School of Materials Science and Engineering, TianGong University, Tianjin 300387, China, Tel. +86 22 83955074; Fax: +86 22 83955055; emails: liguangfen@tjpu.edu.cn (G.F. Li), 294736581@qq.com (G.L. Wang), 1547673352@qq.com (Y.Y. Huan)

Received 26 December 2019; Accepted 23 July 2020

---

### ABSTRACT

Here, a coupling process of grafting and polymerizing of acrylic acid (AA) on multi-walled carbon nanotubes (MWCNTs) was used to prepare modified MWCNTs (PAA-g-MWCNTs), which were then blended at different dosages with polyvinylidene fluoride for obtaining composite membranes via a phase inversion method. The analysis from the membrane morphology, surface hydrophilicity, mechanical properties, permeability and adsorption capacity showed that the best membrane performance was found when the dosage of modified MWCNTs (PAA-g-MWCNTs) was 1.5 wt.%. With the increase of dye initial concentration, adsorption time, temperature and pH, the adsorption capacity of methylene blue (MB) increases gradually. A pronounced effect of pH on the adsorption capacity was especially found from zeta potential analysis. The adsorption data are more in line with the pseudo-second-order kinetic model and the Freundlich isotherm model. The determined corresponding thermodynamic parameters verified that the adsorption is a spontaneous, endothermic and physical process. The adsorption mechanism of MB by the composite membrane suggests that there are many interactions as an electrostatic attraction, hydrogen bonding and  $\pi$ - $\pi$  electron coupling presented between membrane and dye molecules.

*Keywords:* Membrane; Dye adsorption; Carbon nanotube; Acrylic acid; Polyvinylidene fluoride

---

### 1. Introduction

Dyes are widely utilized in many industrial fields, for instance, textiles, clothing, paper, plastics and other industries due to their superior affinity for coloring materials and their characteristics of not easy decolorization and decomposition in use. The extensive application of dyes has produced a large amount of dye wastewater and thus has a great impact on the ecological environment as dye possesses complex cyclic aromatic structure and is difficult to be removed from wastewater [1,2]. Compared with traditional biological and chemical methods, the adsorption is globally recognized as the most promising

method for the removal of synthetic dyes and metal ions from wastewater, because it has many advantages, such as economical, efficient, simple and easy operation [3–5].

Polyvinylidene fluoride (PVDF) is a very popular composite membrane material because of its excellent mechanical properties, thermal properties, chemical resistance and thermodynamic compatibility with other polymers [6]. Moreover, PVDF is soluble in ordinary organic solvents and can be prepared by a simple immersion phase conversion process. However, the surface of the PVDF membrane has strong hydrophobicity, which makes it difficult for dyes in solution to contact the composite membrane. Therefore, hydrophilic modification of the composite membrane is

---

\* Corresponding author.

needed. Common methods include surface coating modification [7], surface grafting modification [8] and interfacial polymerization modification [9], but these methods are complex, costly and polluting the environment. Therefore, it is urgent to find a simple, low-cost and green method to improve the hydrophilicity of composite membranes. Many studies have proved that nanoparticle doping and blending modification is considered as an excellent alternative method [10,11]. And some studies have shown that the nanoparticles incorporated membranes possess not only improved the hydrophilicity and antifouling properties of the composite membranes but also better adsorption and separation properties [12,13]. Zhang et al. [14] prepared modified composite membranes by blending  $\text{TiO}_2$  nanoparticles and polyethylene glycol mixture with PVDF. The results showed that the hydrophilicity and anti-fouling performance of the modified composite membranes were significantly enhanced compared with pure PVDF membranes [14]. Wu et al. [15] increased the hydrophilicity of PVDF membranes by using modified  $\text{SiO}_2$  nanoparticles, which can exist stably in the membrane matrix during its use. Therefore, improving the hydrophilicity and antifouling of PVDF membranes by doping nanoparticles is feasible. Zeng et al. [6] prepared nanofiltration membranes by blending PVDF with modified halloysite nanotubes (A-HNTs). The results showed that the electrostatic interaction between the surface of nanofiltration membranes modified with A-HNTs and dyes was enhanced and the adsorption capacity was improved significantly.

Multi-walled carbon nanotubes (MWCNTs) can increase the mechanical properties of the membranes due to their perfect mechanical properties, while large specific surface area and special interlayer structure can improve the dye adsorption capacity of the membranes [16]. Therefore, MWCNTs have been widely used in the wastewater treatment membrane field. Wasim et al. [17] modified the PVDF membrane with carbon nanotubes and chitosan to make the rejection rate of the membrane as high as 91% for reactive orange 16 dye. Ghaemi et al. [18] found that PES nanofiltration membranes doped with MWCNTs could efficiently adsorb dyes in water. However, the interaction between MWCNTs makes it difficult to disperse in the membrane matrix, surface modification of MWCNTs is required. Carbon nanotubes modification includes physical modification and chemical modification. Physical modification often adopts ball milling and high-speed agitation to obtain shorter carbon nanotubes to improve their dispersion [19,20]. However, physical methods lead to the loss of the advantages of a large aspect ratio of carbon nanotubes, which could not effectively improve the mechanical properties of the membranes. Chemical modification generally includes strong acid and alkali activation and polymer grafting modification [21–24]. Chiang et al. [25] modified MWCNTs with  $\text{H}_2\text{SO}_4/\text{HNO}_3$  and introduced some oxygen-containing groups on the surface of MWCNTs, which made MWCNTs disperse well in solution. But, strong acid and strong alkali treatment can cause corrosion to the surface structure of MWCNTs, which weakens the  $\pi$ - $\pi$  conjugation effect between MWCNTs and aromatic structures in dye molecules and reduces the adsorption effect. At present, some progress has been made in the modification of MWCNTs by graft polymerization. Ma et al. [26] grafted

polymethylmethacrylate onto the surface of MWCNTs to increase their hydrophilicity while improving the compatibility with PVDF membranes [26]. However, the length of the polymer molecular chain and the group in the molecule are prone to produce a steric hindrance effect. On the one hand, it reduces the activity of grafting reaction with MWCNTs, on the other hand, it hinders the contact of dye molecules with the membrane. Therefore, it is a feasible strategy to develop PVDF composite membranes with carbon nanotubes grafted from monomers containing hydrophilic groups for removing dyes from wastewater.

In this study, we innovatively modified MWCNTs with acrylic acid (AA) monomers to acquire PAA-g-MWCNTs (the "PAA" stands for polyacrylic acid) with a large number of adsorption sites, which can not only improve the grafting rate of AA on MWCNTs, but also avoid steric hindrance effect due to the long polymer molecular chain. Then PAA-g-MWCNTs/PVDF composite membranes were prepared by blending PVDF with different dosages of PAA-g-MWCNTs. The prepared PAA-g-MWCNTs and composite membranes were characterized by transmission electron microscopy (TEM), X-ray photoelectron spectroscopy (XPS), Fourier-transform infrared spectroscopy (FTIR), scanning electron microscopy (SEM), mechanical tensile test, water contact angle (CA) and permeability test. The effects of pH, adsorption time, dye solution concentration and temperature on the adsorption properties of composite membranes were researched. In addition, the equilibrium, kinetics and thermodynamic adsorption models of dye adsorption process by the composite membrane were investigated, and the thermodynamic parameters of the adsorption process were deduced.

## 2. Experimental setup

### 2.1. Materials

Polyvinylidene fluoride (PVDF, Mw = 45,000) was acquired from Dongguan Tengda plastic material Co. Ltd., China. Polyvinylpyrrolidone (PVP, Mw = 58,000), N,N-dimethylformamide (DMF,  $\geq 99.5\%$ ) and the materials of phosphate buffer solution (PBS) were supplied by Tianjin Kermel Chemical Reagent Co. Ltd., China. Toluene, sulfuric acid ( $\text{H}_2\text{SO}_4$ , 95%–98%) and nitric acid ( $\text{HNO}_3$ , 65%–68%) were purchased from Tianjin Sailboat Chemical Reagent Technology Co. Ltd., China. Acrylic acid (AA, 98%) and azobisisobutyronitrile (AIBN) were purchased from Shanghai Energy Chemical Technology Co. Ltd., China. Bovine serum albumin (BSA, Mw = 68,000) was bought from Solarbio Science & Technology Co. Ltd., China. Methylene blue (MB, Mw = 373.9) was purchased from Tianjin Guangfu Chemical Research Institute, China.

### 2.2. Preparation of PAA-g-MWCNTs

MWCNTs were modified by in-situ polymerization. The experimental methods were as follows: pure MWCNTs (PMWCNTs, 0.05 g) pre-rinsed by diluted mixed acid ( $\text{H}_2\text{SO}_4:\text{HNO}_3 = 3:1$ ) was dispersed uniformly in toluene solution (40 ml) under ultrasonication. When the water bath temperature reached 60°C, AA (1 mL) monomer and AIBN initiator (0.0105 g) were added to the solution, respectively,

and stirred continuously for 6 h. The samples were filtered by microfiltration membrane with 0.45  $\mu\text{m}$  pore size, then cleaned for several times with deionized water, and then dried in an oven at 60°C for 10 h. Finally, PAA-g-MWCNTs were obtained.

### 2.3. Preparation of PAA-g-MWCNTs/PVDF composite membranes

Pure PVDF membrane (M0) and PAA-g-MWCNTs/PVDF membranes (M1–M4) were fabricated via a method of immersion phase-inversion. The preparation process is shown in Fig. 1.

According to the compositions in Table 1, certain content of PAA-g-MWCNTs and PVP were firstly added into the DMF solvent and the prepared mixture was sonicated for 1 h to obtain a uniform dispersion. Subsequently, the dried PVDF powder was dissolved in the above dispersion and magnetically stirred at 70°C for 6 h. The uniform casting solution was sonicated for 10 min and then placed in a vacuum oven (25°C) for 4 h to remove the bubbles. Afterward, the casting solution was dumped on a glass plate using a 150  $\mu\text{m}$  thickness scraper, then immediately immersed in a coagulation bath. After the membrane was formed, it was placed in a coagulation bath for 48 h to remove residual DMF solvent and complete phase inversion. Finally, the membrane was dried at room temperature for further use.

### 2.4. Characterization of PAA-g-MWCNTs

To observe the surface morphology of carbon nanotubes, TEM (Hitachi H7650, Japan) was used. PMWCNTs and PAA-g-MWCNTs were scattered in ethanol and then evenly dripped on the surface of the microgrid supporting film (300 mesh). FTIR (Thermo Fisher Scientific, USA) was used for the analysis of chemical compositions in the range of 500–4,000  $\text{cm}^{-1}$ . The content of oxygen groups on the surface

of carbon nanotubes was further analyzed by XPS (Thermo Fisher Scientific, USA).

### 2.5. Characterization of the composite membranes

#### 2.5.1. Morphological characterization

The structures of all the samples were investigated by the SEM (Hitachi S4800, Japan). The cross-sectional samples were ruptured in liquid nitrogen and attached to the sample stage and sputtered with gold, then observed at 10 kV.

#### 2.5.2. Porosity and mean pore size

The wet membranes with a size of 50 mm  $\times$  50 mm were weighed ( $W_1$  (g)), they were then dried and weighed again ( $W_2$  (g)). The sample thickness ( $h$  (m)) was measured. Porosity ( $\epsilon$ ) was obtained by Eq. (1) [27]:

$$\epsilon = \frac{W_1 - W_2}{A \times h \times \rho_w} \times 100\% \quad (1)$$

where  $\rho_w$  is the density of deionized water (0.988  $\text{g cm}^{-3}$ ),  $A$  is the effective area of the sample ( $\text{m}^2$ ).

The mean pore radius ( $r_m$ ) was calculated by Eq. (2) [28]:

$$r_m = \sqrt{\frac{(2.9 - 1.75\epsilon) \times 8\mu h Q}{\epsilon \times A \times \text{TMP}}} \quad (2)$$

where  $\mu$  is the viscosity of deionized water ( $8.9 \times 10^{-4}$  Pa s),  $Q$  is the volume of the deionized water per second ( $\text{m}^3 \text{s}^{-1}$ ), TMP is the transmembrane pressure (Pa).

#### 2.5.3. Mechanical properties

The universal testing machine (GMT4000, MTS Systems Co. Ltd., China) was used to measure the mechanical properties

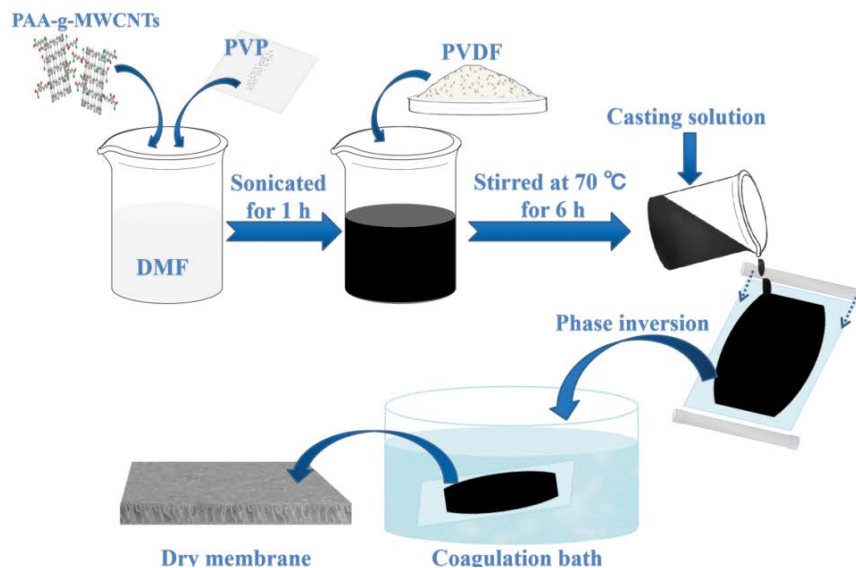


Fig. 1. Schematic illustration of the preparation of PAA-g-MWCNTs/PVDF composite membrane.

Table 1  
Composition and proportion of membrane casting solution

Samples	PVDF (wt.%)	PAA-g-MWCNTs (wt.%)	PVP (wt.%)	DMF (wt.%)
M0	15	0	1	84
M1	15	0.5	1	83.5
M2	15	1	1	83
M3	15	1.5	1	82.5
M4	15	2	1	82

of the membranes. Cut the sample into 30 mm × 5 mm strips and the measurement was carried out at a drawing speed of 15 mm min<sup>-1</sup>. Every sample was tested three times and these data were averaged.

#### 2.5.4. Hydrophilicity

To evaluate the hydrophilicity of the samples, water contact angles (CA) on sample surfaces were measured at room temperature by using the DSA100 drop shape analyzer (Krüss, Germany). The data was collected from five pieces randomly selected for each sample, and then the average was derived to represent the contact angle of the sample.

#### 2.5.5. Permeability characterization

Membrane permeability was tested by a cross-flow system. The required effective membrane area ( $A$  (m<sup>2</sup>)) is  $7.1 \times 10^{-4}$  m<sup>2</sup>. Before the measurement, the system was adjusted to 0.2 MPa and operated for 10 min to stabilize the water flux. Measurements were then taken at 0.1 MPa and fluxes were recorded every 10 min, each measurement was repeated at least three times and these data were then averaged. BSA (1 g) was dissolved in PBS solution (1 L) to obtain a BSA solution, followed by a BSA rejection test at 0.1 MPa. The BSA concentration of the initial and permeated solution was measured by an ultraviolet spectrophotometer (Shimadzu, UV-2450, Japan) at a wavelength of 280 nm. The pure water flux ( $J_w$  (L m<sup>-2</sup> h<sup>-1</sup>)) and BSA rejection ( $R$  (%)) of the membrane is calculated as Eqs. (3) and (4) [29]:

$$J_w = \frac{Q}{A \times t} \quad (3)$$

$$R = \left(1 - \frac{C_p}{C_f}\right) \times 100\% \quad (4)$$

where  $Q$  and  $t$  are the volume of permeation water (L) and time (h), respectively.  $C_p$  and  $C_f$  are the BSA concentration of the initial and permeated solutions (mg L<sup>-1</sup>), respectively.

#### 2.5.6. Zeta potential

The charges of samples were tested by the solid surface zeta potentiometer (SurPASS-3, Anton Paar, Austria) at room temperature. The pH of the standard solution (KCl) flowing through the membrane surface is controlled by regulating

acid (HCl) and base (NaOH) feed. At the moment, the zeta potential on the membrane surface at different pH values was directly monitored [28]. Each test was performed three times and the data at each pH point was then averaged.

#### 2.5.7. Adsorption experiment

Adsorption experiments were performed by placing membrane samples with a size of 40 mm × 40 mm into MB solution (30 mL), which has an initial concentration of 20 mg L<sup>-1</sup>. The sample pieces were firstly weighed ( $m$  (g)), then immersed in the solution at room temperature for a certain time. Subsequently, the variations of solution concentrations were calculated from colorimetrically measured absorbance of MB solution at ( $\lambda_{\max} = 663$  nm) using an ultraviolet spectrophotometer. The adsorption capacity ( $Q_t$  (mg g<sup>-1</sup>)) of MB on the samples at  $t$  time was calculated by the following Eq. (5) [30]:

$$Q_t = \frac{(C_0 - C_t) \times V}{m} \quad (5)$$

where  $C_0$  and  $C_t$  (mg L<sup>-1</sup>) are the initial and  $t$  time concentrations of MB.  $V$  (L) and  $m$  (g) represent the dye volume and the adsorbent mass, respectively.

The membrane with the highest adsorption capacity was then selected for the further studying of the combined effects of adsorption time, solution pH, concentration and temperature on the adsorption capacity. The samples were tested in MB solutions of different pH (2, 4, 6, 8 and 10), concentrations (10, 15, 20, 25 and 30 mg L<sup>-1</sup>) and temperatures (293, 303, 313, 323 and 333 K), respectively. And each set of tests was performed at least three times to prevent errors. The adsorption data of each set of experiments were calculated by the above formula, and then the equilibrium, kinetic, thermodynamic mathematical models and adsorption mechanism were studied.

### 3. Results and discussion

#### 3.1. Characterization of PAA-g-MWCNTs

Figs. 2a and b display TEM images of PMWCNTs and PAA-g-MWCNTs. The surface of PMWCNTs sidewall is quite smooth and the existence of van der Waals force leads to the entanglement of carbon nanotubes. However, the surface of PAA-g-MWCNTs is rougher and the average

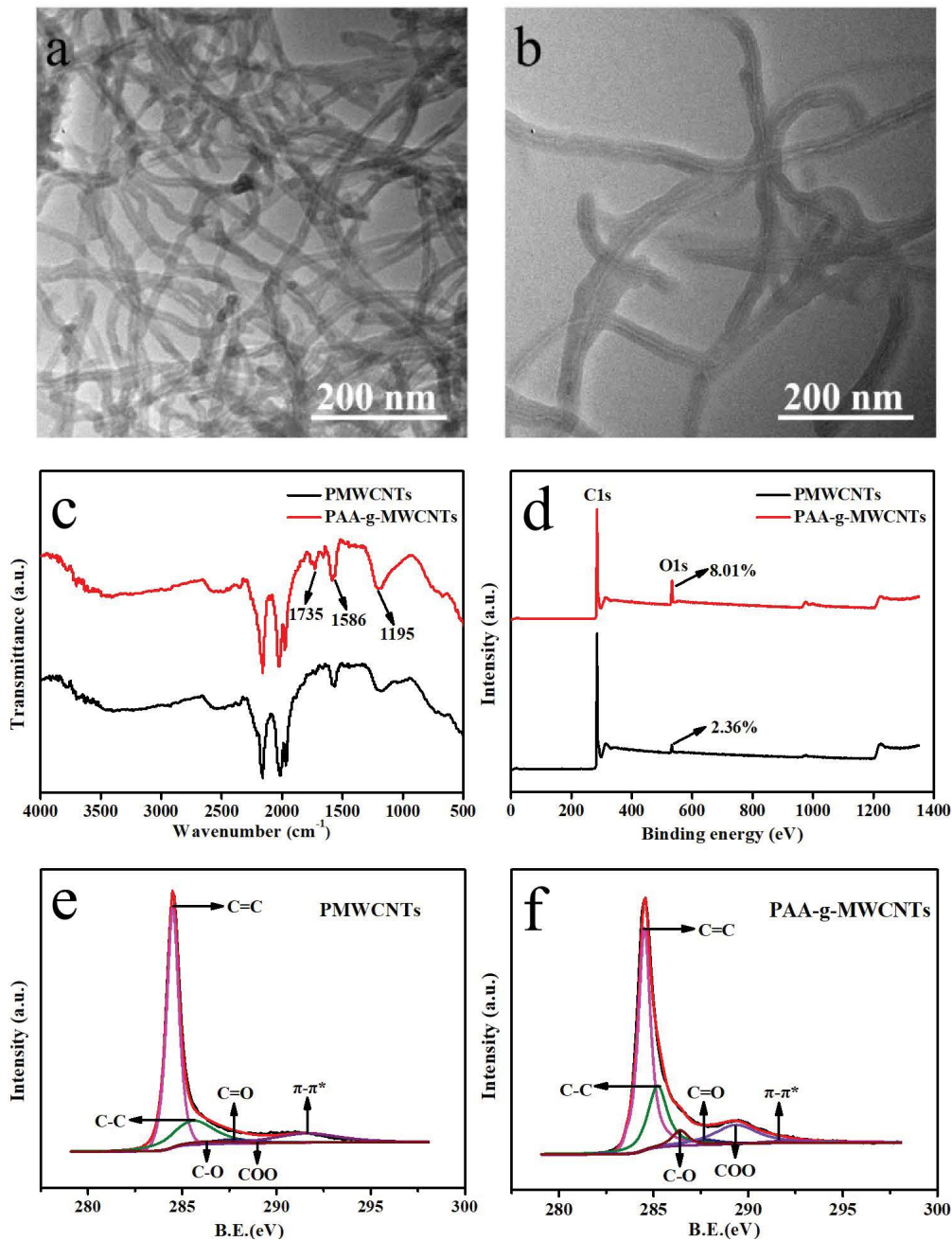


Fig. 2. The TEM images of (a) PMWCNTs, (b) PAA-g-MWCNTs, (c) FTIR, (d) XPS spectra of C and O elements from two samples; XPS C1 spectra of (e) PMWCNTs and (f) PAA-g-MWCNTs.

diameter is larger than that of PMWCNTs. This might result from the attachment of AA onto MWCNTs surfaces.

FTIR and XPS are powerful methods to judge the modification effect of MWCNTs. Fig. 2c shows the FTIR spectra of PMWCNTs and PAA-g-MWCNTs. After modification, the peaks intensity of PAA-g-MWCNTs at 1,586 and 1,195 cm<sup>-1</sup> increases compared with that of PMWCNTs, which are attributed to the stretching vibration of  $-C=C$  and the asymmetric stretching vibration of  $-C-O-C-$ , respectively. The new peak at 1,735 cm<sup>-1</sup> in the spectrum of PAA-g-MWCNTs

corresponds to the stretching vibration of  $-C=O$  [31]. This confirmed that AA was grafted onto the surface of carbon nanotubes. The XPS spectra in Fig. 2d displays that the binding energies of C1s and O1s characteristic peaks of PMWCNTs and PAA-g-MWCNTs are 284.5 and 532.0 eV, respectively. As can be seen from the peak of O1s, the oxygen content of PAA-g-MWCNTs (8.01%) is 3.4 times as much as PMWCNTs (2.36%). Further, Figs. 2e and f exhibited the XPS C1 spectra of PMWCNTs and PAA-g-MWCNTs, respectively. Compared with PMWCNTs, the peak of oxygen-containing

functional groups (COO, C=O, C–O) and C–C of PAA-g-MWCNTs was significantly enhanced, while the peak of C=C was relatively weakened. These results indicated that the successful graft polymerization of AA monomer on the surface of MWCNTs, resulting in the derivation of PAA and the introduction of a large number of carboxyl groups, which is beneficial for improving the dispersion property of carbon nanotubes.

The hydrophilic performance of PMWCNTs and PAA-g-MWCNTs are presented in Fig. 3. It can be seen that two samples were evenly dispersed in water at the beginning. After 7 d, PMWCNTs completely precipitate to the bottom of the glass bottle, while PAA-g-MWCNTs are still uniformly dispersed in water. Furthermore, the contact angle of PAA-g-MWCNTs (31.2°) is lower than that of PMWCNTs (122.1°), which again confirms that AA was successfully grafted onto the surface of MWCNTs. The excellent dispersibility and hydrophilicity of PAA-g-MWCNTs are expected to greatly improve the hydrophilicity of PVDF composite membranes.

### 3.2. Morphology of membranes

The morphology of the surface (a) and the cross-section (b) of the M0–M4 were shown in Fig. 4. Clearly, M0 has a smooth surface with fewer pores (Fig. 4M0-a). As the amount of PAA-g-MWCNTs increases, fine cracks and micropores begin to appear on the membranes surface, as shown in Fig. 4M1-a to M4-a. This is because the hydrophilic modified carbon nanotubes inside the membrane migrated toward the surface of the membrane during phase inversion [32]. The cross-section images of the membranes show that all samples have a typical asymmetric structure. Fig. 4M0-b displays that the pure PVDF membrane possesses a mostly sponge-like pore structure with a small amount of teardrop-like pore structure in the cross-section areas. With the addition of PAA-g-MWCNTs, the sponge-like structure becomes less and the teardrop-like pore gradually becomes longer and wider and eventually forms a finger-like pore structure, as shown in Fig. 4M1-b to M3-b. This is because the presence of PAA-g-MWCNTs increases the diffusion rate of the solvent and water promotes the completion of phase inversion,

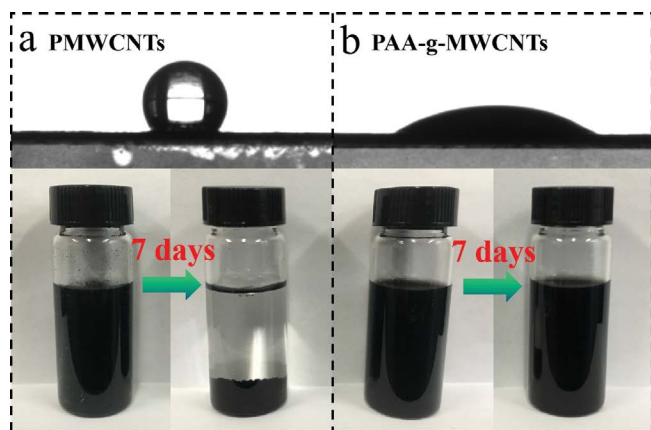


Fig. 3. The contact angle of PMWCNTs and PAA-g-MWCNTs and dispersion properties in water before and after 7 d.

and results in the formation of finger-like holes, which can favor in an enhancement of the membrane porosity.

### 3.3. Porosity and mean pore size, mechanical properties, surface hydrophilicity and permeation properties of membranes

As shown in Fig. 5a, both the porosity and mean pore size of M1–M4 is higher than that of M0. The porosity and mean pore size of M0 are only 45.7% and 23.8 nm, while that of M1–M4 exceeds 62% and 45 nm, respectively. The highest porosity (67.5%) and mean pore size (54.7 nm) are found in sample M3. However, when the content of PAA-g-MWCNTs reached 2 wt.%, macropores with uneven distribution appeared on the membrane surface (Fig. 4M4-a), simultaneously, large holes were observed in the cross-section (Fig. 4M4-b). The excess PAA-g-MWCNTs enhances the viscosity of the system, induces the aggregation of the carbon nanotubes and lowers the phase transformation

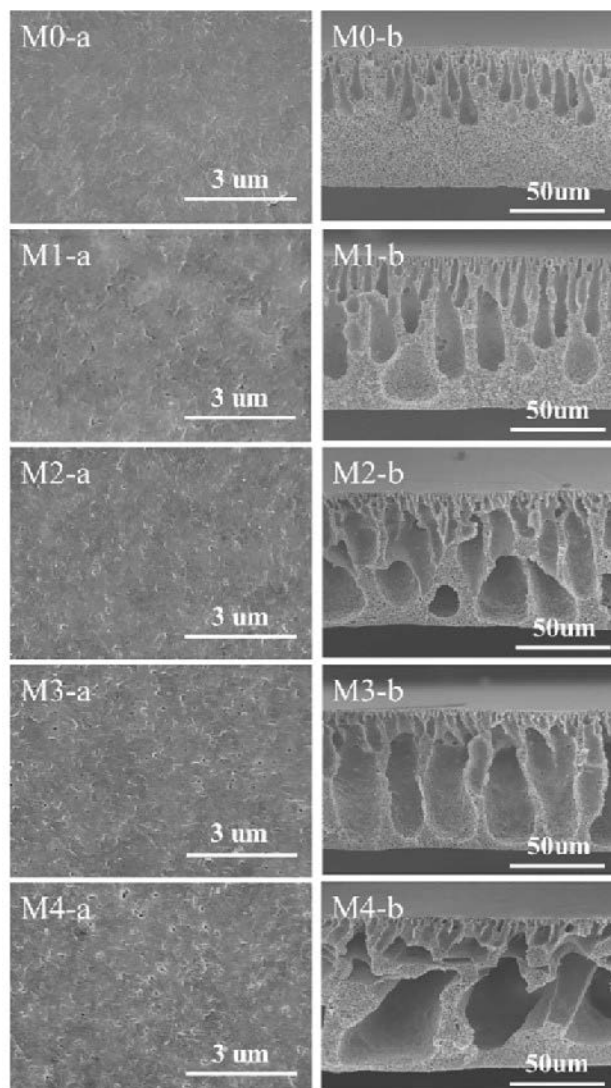


Fig. 4. SEM images of the (a) surfaces and (b) cross-sections of the M0–M4.

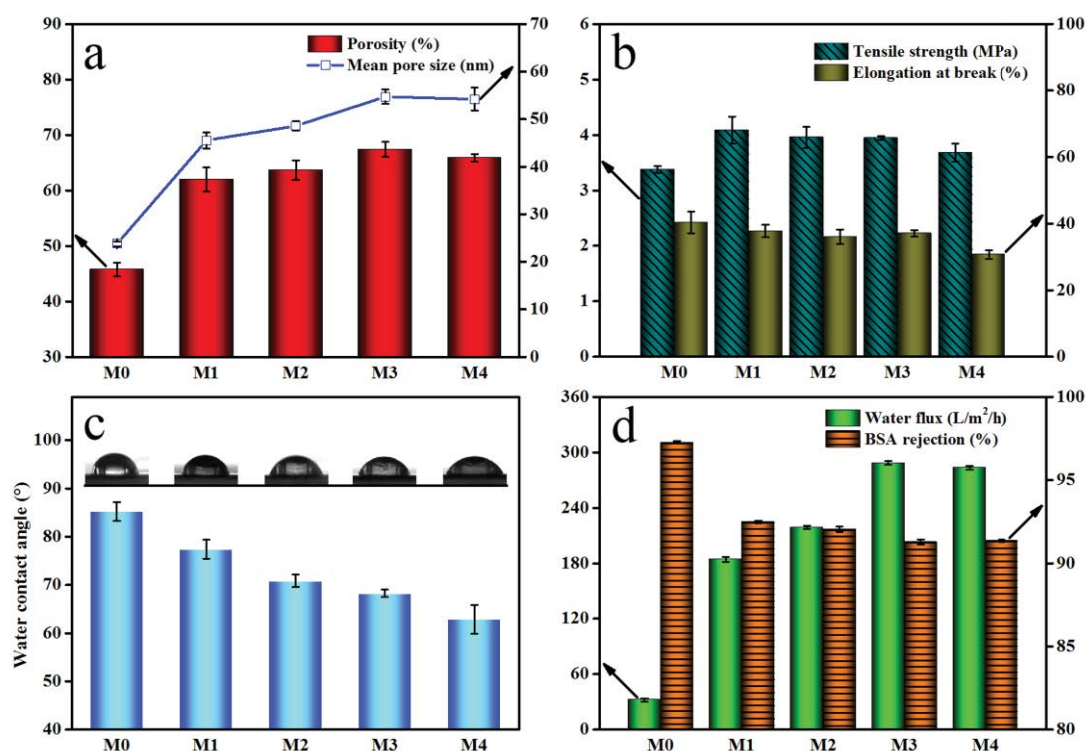


Fig. 5. (a) Porosity and mean pore size, (b) mechanical properties, (c) static water contact angles and (d) pure water flux and BSA rejection for M0–M4.

rate, and finally results in the formation of macropores in the carbon nanotubes aggregation zone during phase inversion.

The mechanical properties of all samples are shown in Fig. 5b. Clearly, the mechanical properties of M1–M4 are superior to those of M0. As the amount of PAA-g-MWCNTs increases, the tensile strength increases from 3.4 to 4.1 MPa, which was 20.6% higher than that of M0, the elongation at break shows a slight decrease compared to M0, indicating a significant increase in tensile strength while substantially maintaining membrane flexibility. The main reason for the improvement of mechanical properties is that PAA-g-MWCNTs can be entangled with the polymer molecular chains, and the effects of multi-crack and pull-out effects are generated when subjected to external forces [33]. However, when the content of PAA-g-MWCNTs is 2 wt.%, the carbon nanotubes are agglomerated due to the strong van der Waals force and the increased viscosity of the system. In addition, the distribution of PAA-g-MWCNTs inside the membrane is uneven, and the formation of defects causes the mechanical properties of the M4 to decrease.

The CA of all samples was shown in Fig. 5c. The initial CA of M0 is around 85.3°, showing the hydrophobicity of the PVDF membrane. With the increased loading of PAA-g-MWCNTs from 0.5, 1, 1.5, to 2 wt.%, the CA gradually decreases to 77.4°, 70.8°, 68.2° and 62.8°, respectively. The hydrophilicity of the composite membranes was ultimately improved because PAA-g-MWCNTs which migrated to the surface of the membranes had good hydrophilicity.

The permeability of the samples was assessed by the pure water flux and BSA rejection and presented in Fig. 5d.

Compared to M0, the water flux of M1–M4 shows an increasing tendency with an increase of PAA-g-MWCNTs content. The water flux of M0 is 32.3 L m<sup>-2</sup> h<sup>-1</sup>, whereas the water flux of M3 is 288.5 L m<sup>-2</sup> h<sup>-1</sup>, which is 8.9 times higher than that of M0. As we all know that water flux has an important relationship with the hydrophilicity and pore structure of the membrane. M0 is not only poor in hydrophilicity, but also has a smooth surface and a dense sponge-like pore in the cross-section, so the water flux is extremely low. The addition of the PAA-g-MWCNTs to M1–M4 membranes improved the hydrophilicity, and a significant change in both type and amount of pore structures in the surface and the cross-section is beneficial of an increase in the membrane porosity. Therefore, the water flux of the composite membranes is significantly improved. The slight decrease of water flux in M4 is caused by the agglomeration of the modified carbon nanotubes and the poor interconnectivity among the pore structures.

The BSA rejection rate of all samples is above 90%. M0 has a smooth surface and is essentially free of micropores, so the rejection can reach 97.3%. The decreases in the BSA rejection for the composite membranes are attributed to the addition of PAA-g-MWCNTs, which facilitates the formation of micropores and finger-like structures during the membrane-forming process, results in an increase of the membrane porosity. The results are similar to those observed from Fig. 5a and are consistent with other studies. The retention capacity of the membrane is based on the sieving mechanism, which is directly correlated to the relative pore size of the membrane surface and the diameter of the BSA particles

### 3.4. Adsorption experiment

#### 3.4.1. Effect of PAA-g-MWCNTs dosage

The effect of PAA-g-MWCNTs dosage on the adsorption performance of M0–M4 was explored in Fig. 6. The adsorption capacity of dye on the membrane M1–M4 increased with the loading of PAA-g-MWCNTs. The  $Q_t$  of M1 and M3 is 2 and 7.5 mg g<sup>-1</sup>, which increased by 2.2 and 8.3 times respectively compared with M0 (0.9 mg g<sup>-1</sup>). Two effects of surface hydrophilicity and porosity are responsible for the improvement of dye adsorption capacity. After adding PAA-g-MWCNTs, the hydrophilicity of the membranes is improved by introducing oxygen-containing functional groups into the membranes, which enhances the electrostatic interaction between dyes and membranes. Moreover, the addition of PAA-g-MWCNTs is conducive to the formation of the pore structure, providing more contact area and contact sites with dyes, thus increasing the dye adsorption.

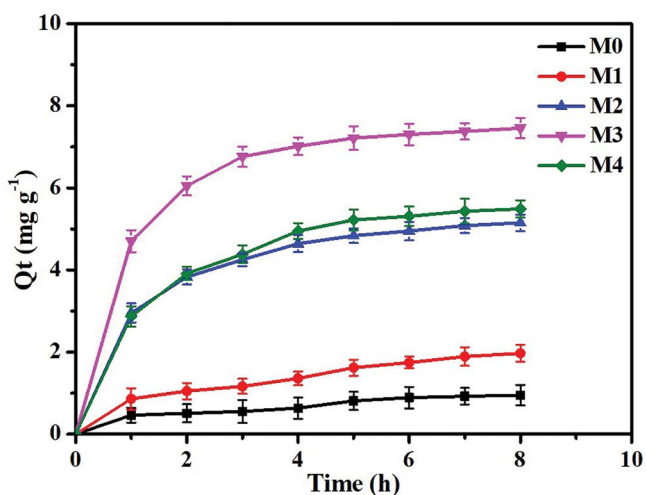


Fig. 6. Effect of PAA-g-MWCNTs dosage on membrane adsorption performance (MB: 20 mg L<sup>-1</sup>; pH = 7, 293 K).

#### 3.4.2. Effect of pH, adsorption time and dye concentration on adsorption behavior

Fig. 7a shows the adsorption curves of M3 in MB solution at different pH values. With the increase of pH, the equilibrium adsorption capacity increased gradually. The  $Q_t$  of M3 increases from 5.1 to 8.5 mg g<sup>-1</sup> as pH varies from 2 to 10, implying a pronounced effect of solution pH on the adsorption properties and the surface charge of the membrane. To verify this, the surface charges of M3 were evaluated by Zeta potential apparatus and compared in Fig. 7a. As the pH value varies from 2 to 10, the surface charge of M3 changes from 6.52 to -56.72 mV. The surface charges turn from positive into negative as the solution changes from acidic into alkaline. Since MB is a cationic dye, when the pH value is 2, the surface of the membrane is positively charged, and the repulsive force between them inhibits the adsorption of MB by the membrane. At the same time, a large amount of H<sup>+</sup> in acidic solution will compete with MB molecules, resulting in low adsorption capacity. However, when the solution is alkaline, the OH<sup>-</sup> in the solution causes massive negative charges on the surface of the membrane, which enhance electrostatic interaction between the membrane and MB and promote the adsorption capacity.

The initial dye concentration and equilibrium adsorption time are important parameters for the design of the wastewater treatment system. Therefore, the adsorption curves of M3 with adsorption time in dye solutions at different initial concentrations were studied and shown in Fig. 7b. All adsorption curves show that  $Q_t$  increased rapidly in the first three hours and then gradually slowed down until the adsorption equilibrium. At the initial stage, there are a large number of adsorption sites on the membrane surfaces and the concentration of dye solution is high. The higher concentration gradient between dye solution and membrane surface allows dye molecules to quickly diffuse to the empty site on membranes. However, at the later stage, the occupied adsorption sites can't accept dye molecules, resulting in the slowing down of the adsorption rate.

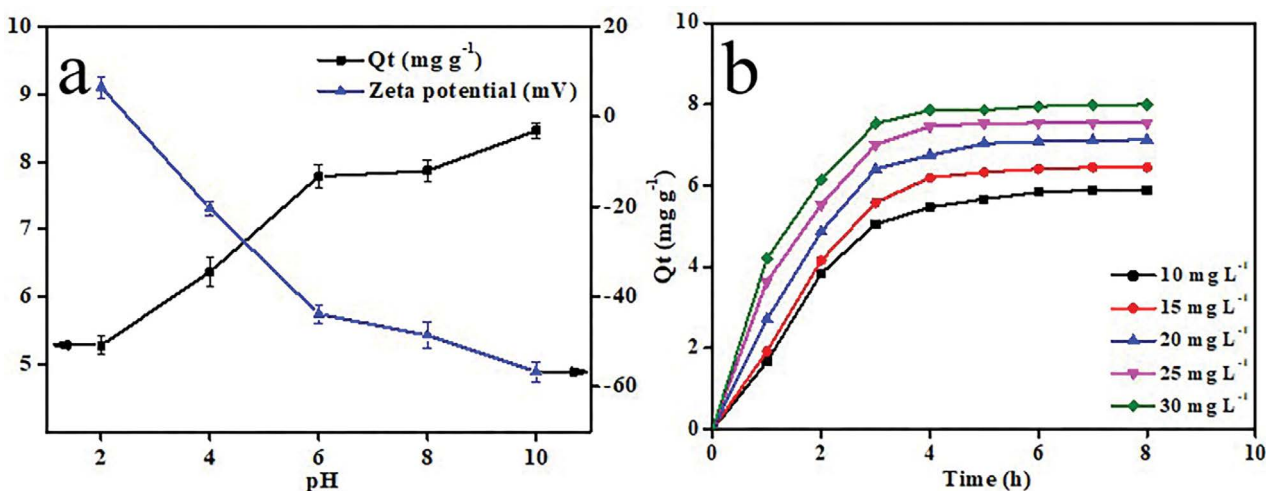


Fig. 7. (a) Influence of solution pH values on the adsorption capacity (MB: 20 mg L<sup>-1</sup>; 293 K) and zeta potential curves of M0 and M3 and (b) adsorption curves of M3 at different MB concentrations and adsorption time (pH = 7, 293 K).

The  $Q_t$  of M3 to dyes increases from 5.9 to 8.0 mg g<sup>-1</sup> with the increase of MB initial concentration changes from 10 to 30 mg L<sup>-1</sup>. Apparently, the concentration gradient in dye solution provides an important driving force to overcome the mass transfer resistance between the water phase and solid phase, and allow more dye molecules in contact with the active sites in the membrane, thus, the  $Q_t$  of MB by the membrane rises with the increase of MB concentration [34].

### 3.4.3. Kinetics study and isotherms study

The adsorption capacity of MB by membrane M3 vs. temperature is illustrated in Fig. 8a. The  $Q_t$  increases from 7.1 to 8.3 mg g<sup>-1</sup> with the temperature from 293 to 333 K. The increase of temperature favors in fast diffusion of the dye molecules to the active sites of the membrane and quickly reaches the adsorption equilibrium, leading to a higher initial adsorption capacity. To reveal the adsorption kinetics of membranes, two non-linear dynamic models are applied in Fig. 8b. The pseudo-first-order and pseudo-second-order dynamic models can be expressed as Eq. (6) and (7) [35]:

$$\ln(Q_e - Q_t) = \ln(Q_e) - k_1 t \quad (6)$$

$$\frac{t}{Q_t} = \frac{1}{k_2 Q_e^2} + \frac{t}{Q_e} \quad (7)$$

where  $t$  (min) is time, and  $Q_t$  and  $Q_e$  (mg g<sup>-1</sup>) refer to the adsorption capacity at  $t$  and equilibrium, respectively.  $k_1$  (min<sup>-1</sup>) and  $k_2$  (g mg<sup>-1</sup> h<sup>-1</sup>) are the rate constants for desorption kinetics.

The value of these fitting parameters and the correlation coefficient ( $R^2$ ) are shown in Table 2. From the  $R^2$  values, the fitting effect between the data and the pseudo-second-order model is higher, implying that the process was more consistent with the pseudo-second-order kinetics model. Simultaneously, this result proves that MB adsorbed by the composite membrane is not an infinite adsorption process and has rapid adsorption to basically reach equilibrium within 4 h.

The former studies clearly show the effects of the initial concentration and temperature on adsorption properties. The adsorption behavior of M3 vs. initial concentration at different temperatures in Fig. 8c demonstrated that the influence of dye concentration on adsorption properties is more predominated compared to temperature. The highest adsorption capacity was 8.7 mg g<sup>-1</sup> for M3, which was placed in MB (30 mg L<sup>-1</sup>) at a temperature of 333 K. Langmuir and Freundlich isotherm adsorption models were utilized to study the adsorption capacity of M3 vs. MB at different concentrations, as shown in Fig. 8d. The Langmuir isotherm assumes that the adsorption is a single layer of coverage and there is no interaction existing among the MB molecules. The Freundlich isotherm can be used for adsorption on non-uniform surfaces, typically for multilayer

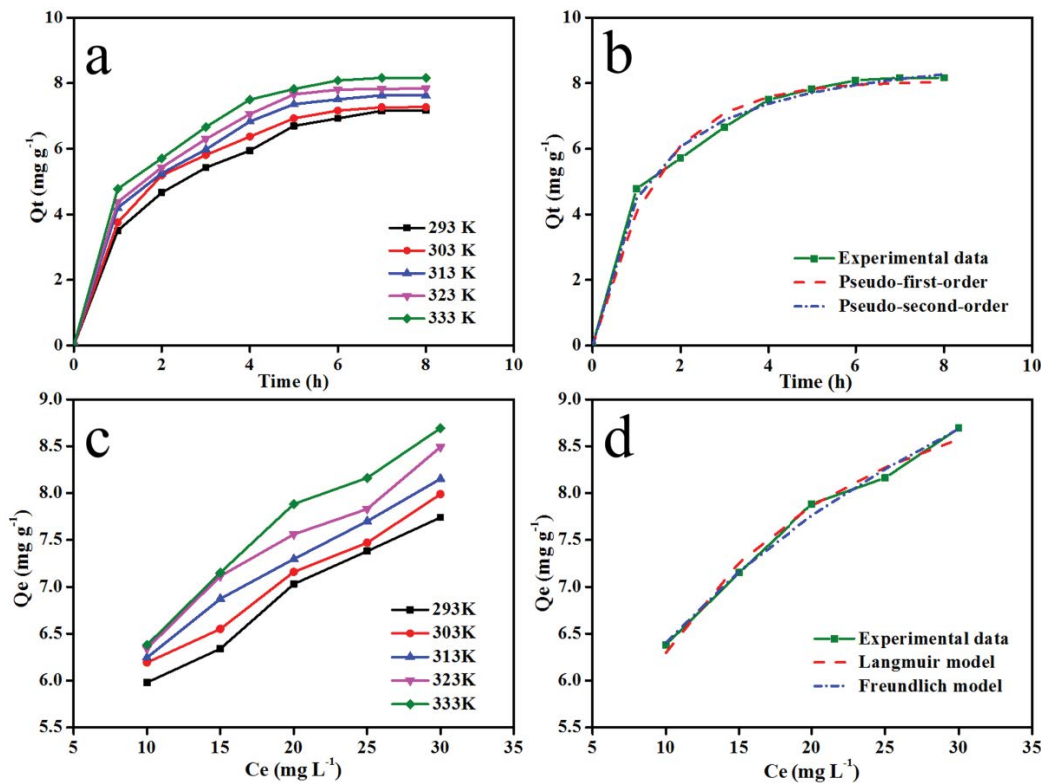


Fig. 8. (a) Influences of temperature on the adsorption performance of M3 under different adsorption time (MB: 20 mg L<sup>-1</sup>; pH = 7), (b) adsorption kinetic models of M3 (MB: 20 mg L<sup>-1</sup>; pH = 7, 333 K), (c) effect of solution concentration on the adsorption performance of M3 under different temperature (pH = 7; adsorption time: 8 h) and (d) adsorption isotherm models of M3 (pH = 7; adsorption time: 8 h; 333 K)

Table 2  
Parameters of two kinetic models

T (K)	Pseudo-first-order model			Pseudo-second-order model		
	$R^2$	$Q_e$ (mg g <sup>-1</sup> )	$k_1$ (min <sup>-1</sup> )	$R^2$	$Q_e$ (mg g <sup>-1</sup> )	$k_2$ (g mg <sup>-1</sup> h <sup>-1</sup> )
293	0.985	7.15	0.536	0.995	8.53	0.068
303	0.991	7.22	0.633	0.998	8.60	0.076
313	0.983	7.58	0.638	0.993	8.97	0.087
323	0.984	7.81	0.654	0.993	9.22	0.094
333	0.982	8.06	0.706	0.994	9.40	0.099

adsorption [36]. The following Eqs. (8) and (9) can describe the above two isotherm models [37]:

$$\frac{C_e}{Q_e} = \frac{1}{Q_m K_L} + \frac{1}{Q_m} C_e \quad (8)$$

$$\ln Q_e = \ln K_F + \frac{1}{n} \ln C_e \quad (9)$$

where  $C_e$  (mg L<sup>-1</sup>) is the concentration of MB at equilibrium;  $Q_m$  (mg g<sup>-1</sup>) is the theoretical saturation capacity of the monolayer (mg g<sup>-1</sup>);  $K_L$  (L mg<sup>-1</sup>) and  $K_F$  [(mg g<sup>-1</sup>)(L mg<sup>-1</sup>)<sup>1/n</sup>] are the correlation indices of the Langmuir and Freundlich isotherm models, respectively;  $n$  is the model reaction constant.

Table 3 lists the derived relevant parameters of the Langmuir and Freundlich isotherm models. As the  $R^2$  of the Freundlich isotherm is higher than that of Langmuir isotherm, the adsorption process of MB by M3 is more consistent with the Freundlich isotherm model. This suggests that the process is in favor of multilayer adsorption due to the interaction between the membrane and dyes and the type of pore structure of the membrane.

Table 4 lists the maximum adsorption capacity to MB dye of PAA-g-MWCNTs/PVDF membrane prepared in this paper and other adsorbents obtained from recent studies. Although the adsorption capacity of PAA-g-MWCNTs/PVDF membrane is lower than that of powder and hydrogel adsorbents, it exhibits high adsorption efficiency under the same experimental conditions as other composite

membrane adsorbents. Meanwhile, PAA-g-MWCNTs/PVDF membrane has excellent mechanical properties and permeability, which all contributed to their wide application in the field of dye wastewater treatment.

#### 3.4.4. Thermodynamic analyses

In order to further estimate the influence of temperature on the adsorption of MB on membranes, the Gibbs free energy of adsorption ( $\Delta G^\circ$ ), enthalpy ( $\Delta H^\circ$ ), entropy changes ( $\Delta S^\circ$ ) and activation energy ( $E_a$ ) were derived to forecast the adsorption process. Since the Freundlich isotherm model is more consistent with the adsorption process than the Langmuir isotherm model, the thermodynamic parameters are calculated by  $K_F$  (L mol<sup>-1</sup>). The calculation equations are as follows [36]:

$$\Delta G^\circ = -RT \ln(K_F) \quad (10)$$

$$\ln(K_F) = \frac{\Delta S^\circ}{R} - \frac{\Delta H^\circ}{RT} \quad (11)$$

$$\Delta G^\circ = \Delta H^\circ - T\Delta S^\circ \quad (12)$$

where  $R$  (8.314 J mol<sup>-1</sup> K<sup>-1</sup>) is the gas constant and  $T$  (K) is the temperature. Eqs. (10) and (11) are organized to obtain Eq. (12),  $\Delta S^\circ$  and  $\Delta H^\circ$  corresponds to the slope and intercept of the equation, respectively.

Thermodynamic parameters obtained at different temperatures are listed in Table 5. It shows that  $\Delta G^\circ < 0$  at all

Table 3  
Parameters of the Langmuir and Freundlich isotherm models at different temperature

T (K)	Langmuir isotherm			Freundlich isotherm		
	$R^2$	$K_L$ (L mg <sup>-1</sup> )	$Q_m$ (mg g <sup>-1</sup> )	$R^2$	$K_F$ [(mg g <sup>-1</sup> )(L mg <sup>-1</sup> ) <sup>1/n</sup> ]	$n$
293	0.928	0.161	9.013	0.977	3.332	4.056
303	0.839	0.165	9.023	0.928	3.501	4.113
313	0.919	0.185	9.352	0.974	3.554	4.159
323	0.846	0.188	9.587	0.904	3.603	4.231
333	0.852	0.195	10.005	0.915	3.625	4.369

temperatures and it turns more negative as the temperature rises up, implying that the adsorption process of MB on the membrane is spontaneous and more intense at high temperatures. The values of  $\Delta H^\circ$  and  $\Delta S^\circ$  are 2.51 kJ mol<sup>-1</sup> and 115.68 J mol<sup>-1</sup> K<sup>-1</sup>, respectively.  $\Delta S^\circ > 0$  indicates that the degree of molecular chaos of MB increases, and the adsorption capacity increases with the increase of the contact probability with the adsorption sites  $\Delta H^\circ > 0$  indicates that this process is endothermic, and it is advantageous to adsorption with the increase of temperature, which is consistent with the increase of adsorption capacity with temperature. The previous study has proposed that  $\Delta H^\circ$  is smaller than 40 kJ mol<sup>-1</sup> for the physical adsorption [47]. The calculation proves that the adsorption of MB on the membrane in this case is a physical process.

$E_a$  (kJ mol<sup>-1</sup>) of the adsorption process was calculated based on the Arrhenius equation. As the kinetic analysis showed that the adsorption of MB molecule on the membrane was more in line with the pseudo-second-order kinetic model,  $k_2$  was taken as the reaction rate constant. The Arrhenius is expressed as Eq. (13) [48]:

$$\ln(K_2) = \ln(A) - \frac{E_a}{RT} \quad (13)$$

where  $A$  is the Arrhenius factor (g mg<sup>-1</sup> h<sup>-1</sup>).

Table 5 shows that the  $E_a$  of the process is 7.88 kJ mol<sup>-1</sup>. The other study announced that the  $E_a$  in the range of 5 to 40 kJ mol<sup>-1</sup> is regarded as physisorption, while the  $E_a$  from 40 to 800 kJ mol<sup>-1</sup> is chemisorption [49]. This result indicates that the barrier of the MB adsorption process is low, and the

process is physical adsorption. Through thermodynamic analysis, we can conclude that the adsorption process in this case is a spontaneous and endothermic physical process.

### 3.4.5. Adsorption mechanism

The SEM images after the composite membrane adsorbing MB are shown in Fig. 9a and b. The broad surface and abundant pore structures of the composite membrane are favorable for MB molecules adsorption. It can be clearly observed that a large number of impurities are distributed on the surface of the composite membrane and in the pore structure of the cross-section, which is the adsorbed MB molecule. Based on the above influencing factors and model analysis, the adsorption mechanism is discussed and displayed in Fig. 9c. The aggregation of MB molecules on the surface and inside is not only due to the large contact area and complex pore structure of the composite membrane, but also due to the complex force field during the adsorption process [50]. The zeta potential test indicates that the composite membrane has an abundant negative charge in the adsorption environment, and MB is a cationic dye, so there is a strong electrostatic attraction between them. Hydrogen bonding is also a force to be considered in organic matter adsorption. Oxygen atoms, fluorine atoms in composite membrane and nitrogen atoms in MB molecules have strong electronegativity, which can form a large number of intermolecular hydrogen bonds with each other's hydrogen atoms [50]. In addition, the free-moving  $\pi$  electrons in the carbon nanotubes in the composite membrane can interact with  $\pi$  electrons in the MB aromatic ring structure to generate  $\pi$ - $\pi$

Table 4  
Maximum adsorption capacity of various adsorbents for MB dye

Adsorbent	Adsorption capacity (mg g <sup>-1</sup> )	Experimental condition	References
PMPC/BNC membrane	4.4	25 mg L <sup>-1</sup> , pH = 6	[38]
PVDF-ZnS pellets	0.5	30 mg L <sup>-1</sup> , pH = 6	[39]
MWCNT-SH	28	40 mg L <sup>-1</sup> , pH = 6	[40]
NH <sub>2</sub> -MWCNTs@Fe <sub>3</sub> O <sub>4</sub>	178.6	100 mg L <sup>-1</sup> , pH = 7	[41]
CMC hydrogel membranes	5	100 mg L <sup>-1</sup> , pH = 5	[42]
MHNTs/PEI membrane	20.4	150 mg L <sup>-1</sup> , pH = 7	[43]
XG-cl-pAA/rGO hydrogel	793.7	200 mg L <sup>-1</sup> , $Q_{max}$	[44]
XG/SiO <sub>2</sub> nanocomposite	448.4	100 mg L <sup>-1</sup> , $Q_{max}$	[45]
SA-cl-poly(AA)-TiO <sub>2</sub> hydrogel	2,257.4	100 mg L <sup>-1</sup> , $Q_{max}$	[46]
PAA-g-MWCNTs/PVDF membrane	8.7	30 mg L <sup>-1</sup> , pH = 7	This work

Note: PMPC: poly(2-methacryloyloxyethyl phosphorylcholine); BNC: bacterial nanocellulose; SH: thiol; CMC: carboxymethylcellulose; MHNT: amine functionalized halloysite nanotubes; PEI: polyetherimide; XG: xanthan gum; SA: sodium alginate; PES: polyether sulfone

Table 5  
Thermodynamic parameters at different temperatures

T (K)	$\Delta G^\circ$ (kJ mol <sup>-1</sup> )	$\Delta H^\circ$ (kJ mol <sup>-1</sup> )	$\Delta S^\circ$ (J mol <sup>-1</sup> K <sup>-1</sup> )	$E_a$ (kJ mol <sup>-1</sup> )
293	-31.54			
303	-32.39			
313	-33.89	2.51	115.68	7.88
323	-34.35			
333	-36.34			

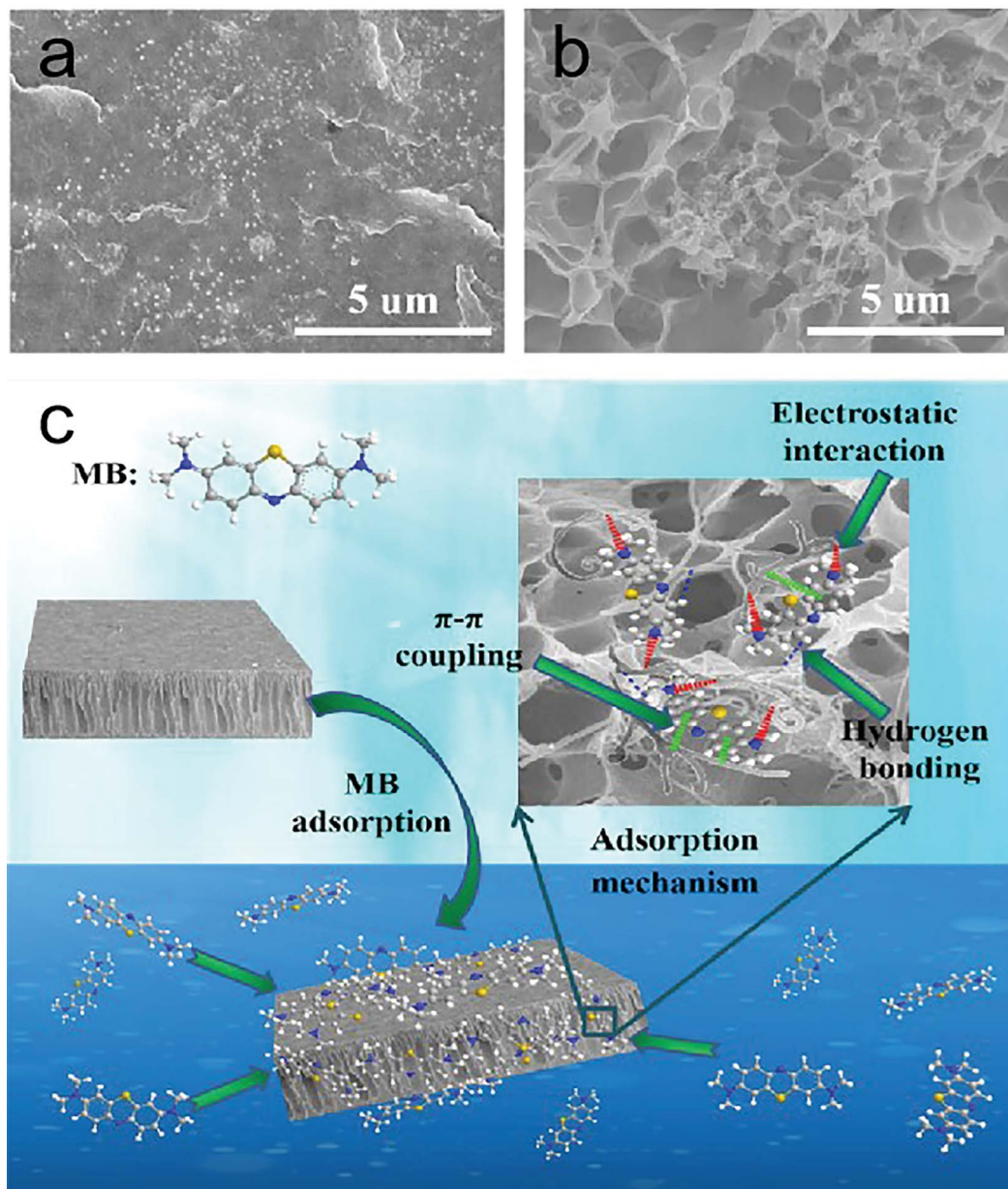


Fig. 9. SEM images of the composite membrane after adsorbing MB (a–b) and adsorption schematic diagram of the composite membrane (electrostatic interaction, hydrogen bonding and  $\pi$ - $\pi$  electron coupling).

electron coupling [51]. Therefore, due to the above multiple forces, MB molecules will spontaneously move towards the composite membrane and aggregate in the surface and pore structure of the composite membrane.

#### 4. Conclusion

Here, the composite membranes of PAA-g-MWCNTs/PVDF were fabricated via the immersion phase inversion method. The attachment of AA onto MWCNTs surface was verified by TEM, FTIR and XPS. Compared with pure PVDF membranes, the hydrophilicity and mechanical properties of PAA-g-MWCNTs/PVDF composite membranes were significantly improved. The SEM images showed that the

composite membranes contain a more finger-like pore structure, which leads to higher porosity and pure water flux. The rejection rate of BSA by all membranes was above 90%. Based on the optimized membrane M3 (PAA-MWCNTs dosage of 1.5 wt.%), the studies revealed that the equilibrium adsorption capacity of the membrane increased with the pH value, adsorption time, initial dye concentration and temperature. The adsorption process was accorded with a pseudo-second-order kinetic model and Freundlich isothermal model. The highest adsorption capacity of  $8.7 \text{ mg g}^{-1}$  was found for M3 at 333 K in dye solution of  $30 \text{ mg L}^{-1}$ , which is attributed to the fast diffusion of dye molecules onto the surface of membranes caused by gradient drove forces from concentration and temperature. In addition,

the thermodynamic analysis shows that the adsorption of MB by the composite membranes is a spontaneous, endothermic, physical process. It is speculated that the adsorption mechanism of MB by the composite membrane to MB includes electrostatic attraction, hydrogen bonding and  $\pi$ - $\pi$  electron coupling.

### Acknowledgment

This research was supported by the National Natural Science Foundation of China (No.51378350) and the Nature Science Foundation of Tianjin City (No.17CTPJC47000).

### References

- [1] G. Crini, Non-conventional low-cost adsorbents for dye removal: a review, *Bioresour. Technol.*, 97 (2006) 1061–1085.
- [2] L.M. Zhou, J.Y. Jin, Z.R. Liu, X.Z. Liang, C. Shang, Adsorption of acid dyes from aqueous solutions by the ethylenediamine-modified magnetic chitosan nanoparticles, *J. Hazard. Mater.*, 185 (2011) 1045–1052.
- [3] E. Makhado, S. Pandey, P.N. Nomngongo, J. Ramontja, Preparation and characterization of xanthan gum-cl-poly (acrylic acid)/*o*-MWCNTs hydrogel nanocomposite as highly effective re-usable adsorbent for removal of methylene blue from aqueous solutions, *J. Colloid Interface Sci.*, 513 (2018) 700–714.
- [4] S. Pandey, J.Y. Do, J. Kim, M. Kang, Fast and highly efficient removal of dye from aqueous solution using natural locust bean gum based hydrogels as adsorbent, *Int. J. Biol. Macromolecules*, 143 (2020) 60–75.
- [5] S. Pandey, J.Y. Do, J. Kim, M. Kang, Fast and highly efficient catalytic degradation of dyes using  $\kappa$ -carrageenan stabilized silver nanoparticles nanocatalyst, *Carbohydr. Polym.*, 230 (2020) 115597.
- [6] G.Y. Zeng, Y. He, Y.Q. Zhan, L. Zhang, Y. Pan, C.L. Zhang, Z.X. Yu, Novel polyvinylidene fluoride nanofiltration membrane blended with functionalized halloysite nanotubes for dye and heavy metal ions removal, *J. Hazard. Mater.*, 317 (2016) 60–72.
- [7] N.G.P. Chew, S.S. Zhao, C. Malde, R. Wang, Polyvinylidene fluoride membrane modification via oxidant-induced dopamine polymerization for sustainable direct-contact membrane distillation, *J. Membr. Sci.*, 563 (2018) 31–42.
- [8] M.N. Goushki, S.A. Mousavi, M.J. Abdekhodaie, M. Sadeghi, Free radical graft polymerization of 2-hydroxyethyl methacrylate and acrylic acid on the polysulfone membrane surface through circulation of reaction media to improve its performance and hemocompatibility properties, *J. Membr. Sci.*, 564 (2018) 762–772.
- [9] Y.F. Li, Y.L. Su, J.Y. Li, X.T. Zhao, R. Zhang, X.C. Fan, J. Zhu, Y.Y. Ma, Y. Liu, Z.Y. Jiang, Preparation of thin film composite nanofiltration membrane with improved structural stability through the mediation of polydopamine, *J. Membr. Sci.*, 476 (2015) 10–19.
- [10] J. Elbert, F. Krohm, C. Rüttiger, S. Kienle, H. Didzoleit, B.N. Balzer, T. Hugel, B. Stühn, M. Gallei, A. Brunsen, Polymer-modified mesoporous silica thin films for redox-mediated selective membrane gating, *Adv. Funct. Mater.*, 24 (2014) 1591–1601.
- [11] X.-D. Zhao, H.-M. Fan, J. Luo, J. Ding, X.-Y. Liu, B.-S. Zou, Y.-P. Feng, Electrically adjustable, super adhesive force of a superhydrophobic aligned MnO<sub>2</sub> nanotube membrane, *Adv. Funct. Mater.*, 21 (2011) 184–190.
- [12] J. Ghobadi, M. Arami, H. Bahrami, N.M. Mahmoodi, Modification of carbon nanotubes with cationic surfactant and its application for removal of direct dyes, *Desal. Water Treat.*, 52 (2014) 4356–4368.
- [13] S.N. Zheng, H.Y. Guo, F.F. Yang, B.Q. Hong, Novel organic dye sorbent: synthesis and adsorption properties of multi-walled carbon nanotubes modified with gallic amide units, *Desal. Water Treat.*, 57 (2016) 12264–12273.
- [14] J. Zhang, Z.C. Wang, X.R. Zhang, X. Zheng, Z.C. Wu, Enhanced antifouling behaviors of polyvinylidene fluoride membrane modified through blending with nano-TiO<sub>2</sub>/polyethylene glycol mixture, *Appl. Surf. Sci.*, 345 (2015) 418–427.
- [15] H. Wu, J. Mansouri, V. Chen, Silica nanoparticles as carriers of antifouling ligands for PVDF ultrafiltration membranes, *J. Membr. Sci.*, 433 (2013) 135–151.
- [16] S.B. Wang, C.W. Ng, W.T. Wang, Q. Li, L.Q. Li, A comparative study on the adsorption of acid and reactive dyes on multiwall carbon nanotubes in single and binary dye systems, *J. Chem. Eng. Data*, 57 (2012) 1563–1569.
- [17] M. Wasim, S. Sagar, A. Sabir, M. Shafiq, T. Jamil, Decoration of open pore network in Polyvinylidene fluoride/MWCNTs with chitosan for the removal of reactive orange 16 dye, *Carbohydr. Polym.*, 174 (2017) 474–483.
- [18] N. Ghaemi, S.S. Madaeni, P. Daraei, H. Rajabi, T. Shojaeimehr, F. Rahimpour, B. Shirvani, PES mixed matrix nanofiltration membrane embedded with polymer wrapped MWCNT: fabrication and performance optimization in dye removal by RSM, *J. Hazard. Mater.*, 298 (2015) 111–121.
- [19] M. Kierkiewicz, E. Pach, A. Santidrián, S. Sandoval, G. Gonçalves, E. Tobias-Rossell, M. Kalbáč, B. Ballesteros, G. Tobias, Comparative study of shortening and cutting strategies of single-walled and multi-walled carbon nanotubes assessed by scanning electron microscopy, *Carbon*, 139 (2018) 922–932.
- [20] K.C. Park, M. Fujishige, K. Takeuchi, S. Arai, S. Morimoto, M. Endo, Inter-collisional cutting of multi-walled carbon nanotubes by high-speed agitation, *J. Phys. Chem. Solids*, 69 (2008) 2481–2486.
- [21] Q. Liao, J. Sun, L. Gao, Adsorption of chlorophenols by multi-walled carbon nanotubes treated with HNO<sub>3</sub> and NH<sub>3</sub>, *Carbon*, 46 (2008) 553–555.
- [22] J. Ma, F. Yu, L. Zhou, L. Jin, M.X. Yang, J.S. Luan, Y.H. Tang, H. Fan, Z.W. Yuan, J.H. Chen, Enhanced adsorptive removal of methyl orange and methylene blue from aqueous solution by alkali-activated multiwalled carbon nanotubes, *ACS Appl. Mater. Interfaces*, 4 (2012) 5749–5760.
- [23] G.D. Sheng, D.D. Shao, X.M. Ren, X.Q. Wang, J.X. Li, Y.X. Chen, X.K. Wang, Kinetics and thermodynamics of adsorption of ionizable aromatic compounds from aqueous solutions by as-prepared and oxidized multiwalled carbon nanotubes, *J. Hazard. Mater.*, 178 (2010) 505–516.
- [24] K.A. Wepasnick, B.A. Smith, K.E. Schrote, H.K. Wilson, S.R. Diegelmann, D.H. Fairbrother, Surface and structural characterization of multi-walled carbon nanotubes following different oxidative treatments, *Carbon*, 49 (2011) 24–36.
- [25] Y.-C. Chiang, W.-H. Lin, Y.-C. Chang, The influence of treatment duration on multi-walled carbon nanotubes functionalized by H<sub>2</sub>SO<sub>4</sub>/HNO<sub>3</sub> oxidation, *Appl. Surf. Sci.*, 257 (2011) 2401–2410.
- [26] W.Z. Ma, Y.C. Zhao, Y.X. Li, P. Zhang, Z. Cao, H. Yang, C.L. Liu, G.L. Tao, F.H. Gong, H. Matsuyama, Synthesis of hydrophilic carbon nanotubes by grafting poly(methyl methacrylate) via click reaction and its effect on poly(vinylidene fluoride)-carbon nanotube composite membrane properties, *Appl. Surf. Sci.*, 435 (2018) 79–90.
- [27] Z.W. Xu, J. Zhang, M.J. Shan, Y.L. Li, B.D. Li, J.R. Niu, B.M. Zhou, X.M. Qian, Organosilane-functionalized graphene oxide for enhanced antifouling and mechanical properties of polyvinylidene fluoride ultrafiltration membranes, *J. Membr. Sci.*, 458 (2014) 1–13.
- [28] X.-S. Yuan, Z.-Y. Guo, H.-Z. Geng, D.S. Rhen, L. Wang, X.-T. Yuan, J. Li, Enhanced performance of conductive polysulfone/MWCNT/PANI ultrafiltration membrane in an online fouling monitoring application, *J. Membr. Sci.*, 575 (2019) 160–169.
- [29] S.W. Li, Z.Y. Cui, L. Zhang, B.Q. He, J.X. Li, The effect of sulfonated polysulfone on the compatibility and structure of polyethersulfone-based blend membranes, *J. Membr. Sci.*, 513 (2016) 1–11.

- [30] Y.J. Yao, H. Bing, X. Feifei, C. Xiaofeng, Equilibrium and kinetic studies of methyl orange adsorption on multiwalled carbon nanotubes, *Chem. Eng. J.*, 170 (2011) 82–89.
- [31] G. Huseyin, Determination of progress in acrylic acid modification on polyvinylidene fluoride membrane by infrared spectroscopy, *J. Mol. Struct.*, 1174 (2018) 122–126.
- [32] S. Panahian, A. Raisi, A. Aroujalian, Multilayer mixed matrix membranes containing modified-MWCNTs for dehydration of alcohol by pervaporation process, *Desalination*, 355 (2015) 45–55.
- [33] Y. Feng, K. Wang, C.H. Davies, H.T. Wang, Carbon nanotube/alumina/polyethersulfone hybrid hollow fiber membranes with enhanced mechanical and anti-fouling properties, *Nanomaterials (Basel)*, 5 (2015) 1366–1378.
- [34] J.L. Gong, B. Wang, G.M. Zeng, C.P. Yang, C.G. Niu, Q.Y. Niu, W.J. Zhou, Y. Liang, Removal of cationic dyes from aqueous solution using magnetic multi-wall carbon nanotube nanocomposite as adsorbent, *J. Hazard. Mater.*, 164 (2009) 1517–1522.
- [35] C.H. Wu, Adsorption of reactive dye onto carbon nanotubes: equilibrium, kinetics and thermodynamics, *J. Hazard. Mater.*, 144 (2007) 93–100.
- [36] C.H. Wu, Studies of the equilibrium and thermodynamics of the adsorption of Cu<sup>(2+)</sup> onto as-produced and modified carbon nanotubes, *J. Colloid Interface Sci.*, 311 (2007) 338–346.
- [37] Y.J. Yao, F.F. Xu, M. Chen, Z.X. Xu, Z.W. Zhu, Adsorption behavior of methylene blue on carbon nanotubes, *Bioresour. Technol.*, 101 (2010) 3040–3046.
- [38] C. Vilela, C. Moreirinha, A. Almeida, A.J.D. Silvestre, C.S.R. Freire, Zwitterionic nanocellulose-based membranes for organic dye removal, *Materials*, 12 (2019) 1404.
- [39] J. Guo, S. Khan, S.-H. Cho, J. Kim, Preparation and immobilization of zinc sulfide (ZnS) nanoparticles on polyvinylidene fluoride pellets for photocatalytic degradation of methylene blue in wastewater, *Appl. Surf. Sci.*, 473 (2019) 425–432.
- [40] D. Robati, B. Mirza, R. Ghazisaeidi, M. Rajabi, O. Moradi, I. Tyagi, S. Agarwal, V.K. Gupta, Adsorption behavior of methylene blue dye on nanocomposite multi-walled carbon nanotube functionalized thiol (MWCNT-SH) as new adsorbent, *J. Mol. Liq.*, 216 (2016) 830–835.
- [41] T. Ahamad, M. Naushad, G.E. Eldesoky, S.I. Al-Saeedi, A. Nafady, N.S. Al-Kadhi, A.a.H. Al-Muhtaseb, A.A. Khan, A. Khan, Effective and fast adsorptive removal of toxic cationic dye (MB) from aqueous medium using amino-functionalized magnetic multiwall carbon nanotubes, *J. Mol. Liq.*, 282 (2019) 154–161.
- [42] N.S.V. Capanema, A.A.P. Mansur, H.S. Mansur, A.C. de Jesus, S.M. Carvalho, P. Chagas, L.C. de Oliveira, Eco-friendly and biocompatible cross-linked carboxymethylcellulose hydrogels as adsorbents for the removal of organic dye pollutants for environmental applications, *Environ. Technol.*, 39 (2018) 2856–2872.
- [43] R.S. Hebbbar, A.M. Isloor, Inamuddin, M.S. Abdullah, A.F. Ismail, A.M. Asiri, Fabrication of polyetherimide nanocomposite membrane with amine functionalized halloysite nanotubes for effective removal of cationic dye effluents, *J. Taiwan Inst. Chem. Eng.*, 93 (2018) 42–53.
- [44] E. Makhado, S. Pandey, J. Ramontja, Microwave assisted synthesis of xanthan gum-cl-poly (acrylic acid) based-reduced graphene oxide hydrogel composite for adsorption of methylene blue and methyl violet from aqueous solution, *Int. J. Biol. Macromol.*, 119 (2018) 255–269.
- [45] S. Thakur, S. Pandey, O.A. Arotiba, Sol-gel derived xanthan gum/silica nanocomposite-a highly efficient cationic dyes adsorbent in aqueous system, *Int. J. Biol. Macromol.*, 103 (2017) 596–604.
- [46] S. Thakur, S. Pandey, O.A. Arotiba, Development of a sodium alginate-based organic/inorganic superabsorbent composite hydrogel for adsorption of methylene blue, *Carbohydr. Polym.*, 153 (2016) 34–46.
- [47] M. Kara, H. Yuzer, E. Sabah, M.S. Celik, Adsorption of cobalt from aqueous solutions onto sepiolite, *Water Res.*, 37 (2003) 224–232.
- [48] M. Dogan, M. Alkan, Adsorption kinetics of methyl violet onto perlite, *Chemosphere*, 50 (2003) 517–528.
- [49] H. Nollet, M. Roels, P. Lutgen, P. Van der Meeren, W. Verstraete, Removal of PCBs from wastewater using fly ash, *Chemosphere*, 53 (2003) 655–665.
- [50] K. Yang, B.S. Xing, Adsorption of organic compounds by carbon nanomaterials in aqueous phase: polanyi theory and its application, *Chem. Rev.*, 110 (2010) 5989–6008.
- [51] B. Pan, B. Xing, Adsorption mechanisms of organic chemicals on carbon nanotubes, *Environ. Sci. Technol.*, 42 (2008) 9005–9012.